archives
of thermodynamics
Vol. **35**(2014), No. 2, 65–92
DOI: 10.2478/aoter-2014-0014

Radiation heat transfer model using Monte Carlo ray tracing method on hierarchical ortho-Cartesian meshes and non-uniform rational basis spline surfaces for description of boundaries

PAWEŁ KUCZYŃSKI[a 1]
RYSZARD BIAŁECKI[b]

[a] Institute of Power Engineering — Research Institute, Thermal Division, Augustówka 36, 02-981 Warszawa, Poland

[b] Silesian University of Technology, Institute of Heat Engineering, Konarskiego 22, 44-100 Gliwice, Poland

Abstract The paper deals with a solution of radiation heat transfer problems in enclosures filled with nonparticipating medium using ray tracing on hierarchical ortho-Cartesian meshes. The idea behind the approach is that radiative heat transfer problems can be solved on much coarser grids than their counterparts from computational fluid dynamics (CFD). The resulting code is designed as an add-on to OpenFOAM, an open-source CFD program. Ortho-Cartesian mesh involving boundary elements is created based upon CFD mesh. Parametric non-uniform rational basis spline (NURBS) surfaces are used to define boundaries of the enclosure, allowing for dealing with domains of complex shapes. Algorithm for determining random, uniformly distributed locations of rays leaving NURBS surfaces is described. The paper presents results of test cases assuming gray diffusive walls. In the current version of the model the radiation is not absorbed within gases. However, the ultimate aim of the work is to upgrade the functionality of the model, to problems in absorbing, emitting and scattering medium projecting iteratively the results of radiative analysis on CFD mesh and CFD solution on radiative mesh.

Keywords: Radiation heat transfer; Monte Carlo; Ray traing; NUBRS surfaces

[1]Corresponding Author. E-mail: pawelkuczy@yahoo.com

Nomenclature

A	–	surface area, m^2
C	–	CFD mesh cell; cell center
D	–	radiation distribution factor
$\mathbf{d}$	–	bundle direction vector
f	–	user-defined surface flatness criterion
h	–	heat transfer coefficient, $\mathrm{W/m^2K}$
$\mathbf{J}$	–	Jacobi matrix
k	–	conductivity, $\mathrm{W/m\,K}$
N	–	number of bundles
$\mathbf{n}$	–	unit normal vector
$\mathbf{o}$	–	bundle origin
p	–	calculated surface flatness
Q	–	heat flux, W
q	–	heat flux per unit area, $\mathrm{W/m^2}$
q_v	–	volumetric heat source, $\mathrm{W/m^3}$
q_r	–	radiative heat flux, $\mathrm{W/m^2}$
R	–	random number from $< 0, 1 >$
S, S_u, S_v	–	parametric surface and its directional derivatives in u and v directions
T	–	temperature, K
t	–	parameter
u, v	–	parametric surface local parameter
V	–	ortho-Cartesian cell

Greek symbols

α	–	absorptivity
δ_{ij}	–	Kronecker delta
ϵ	–	emissivity
σ	–	Stefan-Boltzmann constant, $\mathrm{W/(m^2K^4)}$

Subscripts

a	–	absorbed
e	–	emitted
i	–	index
ij	–	from surface element i to surface element j
j	–	index
n	–	iteration number

1 Introduction

Modeling of radiation heat transfer is a challenging task because of the nature of the process in which each surface and volume can interact with each other on large distances. The problem complicates even more if specular reflections and wavelength varying properties of surfaces and gases are taken

into account. Monte Carlo is a method which can deal with problems of high complexity while keeping the code of the program relatively simple [1, 2]. Although very versatile, the method is computationally expensive since it requires tracing a huge number of rays. On the other hand, the algorithm of ray tracing is a good candidate for parallel computation [3], because the tracing procedure does not need any information about the fate of other rays.

The paper presents system for Monte Carlo ray tracing (MCRT) utilizing coarse ortho-Cartesian mesh which is created based upon computational fluid dynamics (CFD) mesh. Parametric non-uniform rational basis spline (NURBS) [14,15] surfaces are used to define enclosure boundaries. The current version of the model does not account for radiation absorption/emission within gases. The code is designed as an add-on to open-source program OpenFOAM [4].

In this case ortho-Cartesian mesh cells are volume elements involved in heat transfer and for which volume heat sources are computed. The volume heat sources correspond to the energy emitted/absorbed by the medium. In order to find the ray absorption point, the information about the length of ray within the medium is needed. As a consequence of using ortho-Cartesian mesh, the volume elements are always axis-aligned parallelepipeds and the procedure of finding the ray-cell intersection is fast and simple to implement [5–9]. The presented model implements uniform ortho-Cartesian mesh, in which the ray is traced cell-by-cell and the ray traverses the space linearly in time. Similar concepts has been presented in the literature, such as uniform space division (USD) [10] and volume by volume advancement (VVA) [11] methods but without NURBS surfaces for the boundary description. It should be emphasized that in case of nonabsorbing/emitting medium the proposed method may not be an optimal one in comparison with other space subdivision methods like octrees, binary space partioning (BSP), k-dimensional trees (KD) or bounding volume hierarchy (BVH). In those approaches the space can be traversed faster than linearly in time. More information about mentioned above methods can be found in [5–7, 12, 13].

In order to specify the boundaries of the enclosure, parametric NURBS surfaces were chosen due to a few reasons. NURBS surfaces are able to describe shapes of high complexity, use little of computer memory and are widely used in CAD programs and computer graphics [14, 15]. Moreover, there exist efficient algorithms for finding ray-NURBS surface intersection.

Most of these algorithms were developed for the purposes of surfaces visualization and rendering in computer graphics.

According to Pabst [16], the algorithms for finding ray-parametric surface intersection can be classified as follows: subdivision, numerical, algebraic, and Bézier clipping.

Subdivision-based algorithms make use of convex hull property of parametric surfaces [17, 18]. The surface is tested for the intersection with ray and in case of success it is subdivided. The process is repeated until no hit is reported or the surface is smaller than the prescribed threshold and therefore is assumed to adequately approximate the real intersection point.

The core of numerical algorithms is the iterative Newton's method characterized by a quadratic convergence rate, provided it has a good initial guess. The algorithm was first used in the context of finding ray-parametric surface intersection by Toth [19]. The initial guesses for Newton's method were obtained from the interval analysis of the surface. Other authors [16, 20–22] used hierarchies of axis aligned bounding boxes to properly initialize Newton's method and to limit the number of ray-surface intersection tests, but they implemented different algorithms for bounding the box creation.

Algebraic method for ray-parametric surface intersection was first demonstrated by Kajiya [23]. The method requires finding the roots of 18th-degree polynomial and is limited to 3rd order surfaces without possibility to extend it to arbitrary NURBS surfaces making it impractical to implement.

The Bézier clipping algorithm for ray-patch intersection was introduced by Nishita [24] and it can be thought of as an integration of subdivision-based and numerical algorithms. The method utilizes convex hull property of parametric patches to determine parts of surface that cannot contain intersection point. The algorithm has better convergence than subdivision-based algorithms and was improved by Efremov [25]. Wang [26] improved the performance of ray-parametric patch intersection algorithm for coherent rays by combining Newton's and Bézier clipping methods.

From the algorithms presented above only Newton's and Bézier clipping methods are fast enough to be implemented in ray tracing. Newton's method has an advantage over the Bézier Clipping, as it is not limited only to Bézier patches and therefore this technique was used in this work.

The following sections concern the detailed description of the MCRT model (Section 2), examples of usage of the model (Section 3) and summary/conclusions (Section 4).

2 Model description

The radiation heat transfer model presented in this paper employs method of radiation distribution factors described by Mahan [1].

2.1 The radiation distribution factor

The radiation distribution factor from the surface element i to surface element j is defined as a fraction of total radiation emitted from the surface element i that is absorbed by element j, Q_{ij}, due to direct radiation and to all possible reflections within the enclosure, Q_i, [1]:

$$D_{ij} = \frac{Q_{ij}}{Q_i} \, . \tag{1}$$

Elements of the distribution factor matrix have the following properties:

1. Conservation of energy

$$\sum_{j=1}^{n} D_{ij} = 1.0 \, , \quad 1 \leqslant i \leqslant n \, . \tag{2}$$

2. Reciprocity

$$\epsilon_i A_i D_{ij} = \epsilon_j A_j D_{ji} \, , \quad 1 \leqslant i \leqslant n, \; 1 \leqslant j \leqslant n \, . \tag{3}$$

3. Combination of conservation of energy and reciprocity

$$\sum_{i=1}^{n} \epsilon_i A_i D_{ij} = \epsilon_j A_j \, , \quad 1 \leqslant j \leqslant n \, . \tag{4}$$

The solution of the radiation heat transfer problem in case of gray diffusive walls without absorbing/emitting medium and known wall temperatures are radiative heat fluxes on the walls

$$q_i = q_{i,e} - q_{i,a} = \epsilon_i \sum_{j=1}^{n} \sigma T_j^4 \left(\delta_{ij} - D_{ij} \right) \, , \tag{5}$$

where: n – number of surface elements, ϵ – total hemispherical emissivity, A – surface area, T – temperature, δ_{ij} – Kronecker delta.

2.2 Monte Carlo ray tracing method

A procedure for calculating values of radiation distribution factors is the core of MCRT method. The elements of radiation distribution factor matrix are estimated by registration of absorption points of energy bundles, that are emitted from each surface element i taking into account reflections, according to the following equation [1]

$$D_{ij} \cong \frac{N_{ij}}{N_i} \,, \tag{6}$$

where: N_{ij} – number of energy bundles emitted in element i and absorbed in element j, N_i – total number of energy bundles emitted from element i. The propagation of the energy bundle is described by a parametric vector equation

$$\mathbf{r}(t) = \mathbf{o} + \mathbf{d} \cdot t \,, \tag{7}$$

where: $\mathbf{o}$ – vector of origin, $\mathbf{d}$ – vector of direction of the energy bundle, t – line parameter. Absorption of the energy bundle at the surface element i occurs when the following condition is fulfilled:

$$R_\alpha < \alpha_i \,, \tag{8}$$

where: α_i – wall absorptivity, R_α – random number from the $\langle 0, 1\rangle$ interval.

For diffuse surfaces the bundle emission or reflection direction is defined by polar and azimuth angles ϕ and θ at a given point:

$$\phi = 2\pi R_\phi \,, \tag{9}$$

$$\theta = \arcsin(\sqrt{R_\theta}) \,, \tag{10}$$

where R_ϕ and R_θ – random numbers from $\langle 0, 1\rangle$ interval.

2.2.1 Ray tracing on ortho-Cartesian mesh

The idea is to create regular ortho-Cartesian mesh (USD, [10]) on which the radiation heat transfer is solved and which communicates with CFD mesh. The ortho-Cartesian mesh cells are therefore parallelepipeds with all walls parallel to the planes of global coordinate system. The communication between both meshes is assured by the fact that every ortho-Cartesian cell contains a list of CFD cells. A given CFD cell belongs to ortho-Cartesian cell if its center is inside the ortho-Cartesian cell. Depending on the type

and number of CFD cells on the list the ortho-Cartesian cells are classified as follows: active – when the list is not empty, boundary – when at least one CFD cell from the list is a boundary cell, inactive - when the list is empty (Fig. 1).

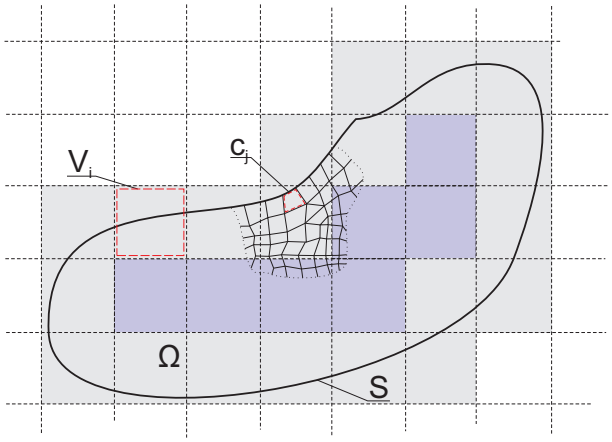

Figure 1: Ortho-Cartesian mesh cells (V_i) created on the basis of CFD mesh cells (C_j): dark – active inner cells, bright – active boundary cells (containing boundary S of domain Ω), white – inactive cells.

The construction of ortho-Cartesian mesh, selection of CFD cells and creation of NURBS surfaces run in preprocessing stage. Thus it is done once for the simulation. The two-way communication between two meshes is realized in the following form: from CFD to ortho-Cartesian mesh the temperature and emissivity of walls are exported and from ortho-Cartesian to CFD mesh the radiative heat flux at walls is exported. Geometrical properties of regular ortho-Cartesian mesh allow using efficient ray tracing algorithm [5–7] and computing values of radiation distribution factors. The algorithm computes the closest ray-cell intersection point and assigns a direction flag to it. In the next step the ray goes to the neighbouring cell according to the direction shown by the flag. In case the ray hits the boundary cell, the procedure for finding the ray-surface intersection point is invoked. If the ray-surface intersection point is found the ray is checked for absorption (8). In case of reflection, new bundle direction is computed from Eqs. (9) and (10). The procedure continues till the ray is absorbed at the surface, i.e., at a boundary element.

2.2.2 Boundary cells of ortho-Cartesian mesh

Boundary cells are special kind of cells, because they contain boundary elements that describe the enclosure geometry. It is assumed that each boundary cell contains exactly one boundary element, which in turn consists of many NURBS surfaces (at least one). At first NURBS surfaces of order 3 are created (one for each boundary cell of ortho-Cartesian mesh) using method of squared distance minimization and boundary points extracted from CFD cells belonging to ortho-Cartesian cells. After the surface 'flattening' procedure (see Section 2.2.4) some of the surfaces are divided and therefore one boundary element can consist of more than one surface. NURBS surfaces of order 3 are flexible enough to express most of complex shapes adequately and the surface evaluation time is acceptable. Moreover, they are widely used in computer graphics and CAD programs [14, 15]. The algorithms for NURBS surface creation from unorganized cloud of points and for surface evaluation were taken from the Point Cloud Library (PCL) [27]. The boundary CFD cells for boundary points extraction are selected using ortho-Cartesian cells overlapping (Fig. 2). The idea was introduced in order to assure the boundaries to be sealed and to avoid creation of NURBS surfaces from too few points. The cells overlapping is defined by parameter OF according to equation

$$OF = \frac{0.5(dx' - dx)}{dx} = \frac{0.5(dy' - dy)}{dy} = \frac{0.5(dz' - dz)}{dz} , \qquad (11)$$

where dx, dy, dz and dx', dy', dz' are ortho-Cartesian cell dimensions before and after introduction of cell overlapping.

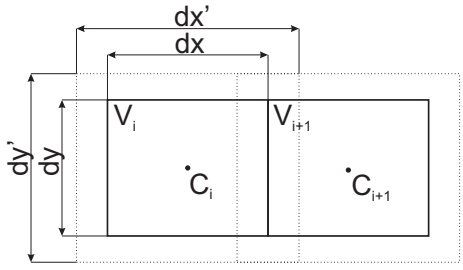

Figure 2: Overlapping of ortho-Cartesian cells V_i and V_{i+1} in order to extract boundary points for NURBS surface creation: dx, dy and dx', dy' – cell dimensions before and after introduction of cell overlapping, C_i, C_{i+1} – cell centers.

2.2.3 Iterative Newton's method

The procedure for finding the ray-surface intersection point is triggered as soon as the ray hits the boundary cell of ortho-Cartesian mesh. It uses iterative Newton's method and bounding volume hierarchy for proper initialization.

The Newton's method has a quadratic convergence rate provided it was given an initial guess (u_0, v_0) that is close enough to the solution. The proper initial guess for the Newton's method is assured by the traversal of the ray through the hierarchy of bounding boxes. The method requires computation of the directional derivatives of the surface at a given point, therefore the surface has to be differentiable in the considered domain. According to [20, 23] the ray equation can be rewritten as an intersection of two planes π_1 i π_2

$$\pi_i : \mathbf{P}_i \cdot (\mathbf{n}_i, d_i) = 0 \,, \quad i = 1, 2 \,. \tag{12}$$

Vectors $\mathbf{P}_1$, $\mathbf{P}_2$ are defined in homogeneous coordinate system by arbitrary, perpendicular unit vectors $\mathbf{n}_1$, $\mathbf{n}_2$ and distances from the coordinate system origin d_1, d_2:

$$\mathbf{P}_i = (\mathbf{n}_i, d_i) \,, \quad i = 1, 2 \,, \tag{13}$$

where

$$d_i = -\mathbf{n}_i \cdot \mathbf{o} \,, \quad i = 1, 2 \,. \tag{14}$$

Ray-surface intersection point $S(u, v)$ can be expressed by

$$\mathbf{P}_i \cdot \big(S(u, v), d_i\big) = 0 \,, \quad i = 1, 2 \,. \tag{15}$$

Inserting Eq. (13) to (15) yields a system of equations

$$\mathbf{F}(u, v) = \begin{pmatrix} \mathbf{n}_1 \cdot S(u, v) + d_1 \\ \mathbf{n}_2 \cdot S(u, v) + d_2 \end{pmatrix} \,, \tag{16}$$

in which the parameters of intersection point u^*, v^* are unknown. Newton's method uses truncated Taylor expansion for the function

$$\begin{pmatrix} u_{n+1} \\ v_{n+1} \end{pmatrix} = \begin{pmatrix} u_n \\ v_n \end{pmatrix} - \mathbf{J}^{-1}(u_n, v_n) \cdot \mathbf{F}(u_n, v_n) \,, \tag{17}$$

where $\mathbf{J}$ is Jacobi matrix of system of equations $\mathbf{F}$ and is defined by

$$\mathbf{J} = (\mathbf{F}_u, \mathbf{F}_v) = \begin{pmatrix} \mathbf{n}_1 \cdot S_u(u, v) \\ \mathbf{n}_2 \cdot S_v(u, v) \end{pmatrix} \,. \tag{18}$$

Vectors S_u, S_v are directional derivatives in u, v directions of parametric surface $S(u, v)$:

$$S_u = \frac{\partial S(u,v)}{\partial u} , \quad S_v = \frac{\partial S(u,v)}{\partial v} . \tag{19}$$

The exit conditions for Newton's iteration are:

1. Convergence
$$||\mathbf{F}(u_n, v_n)|| < \epsilon . \tag{20}$$
2. Divergence
$$||\mathbf{F}(u_{n+1}, v_{n+1})|| > ||\mathbf{F}(u_n, v_n)|| . \tag{21}$$
3. Exceeding maximum number of iterations n_{max}
$$n > n_{max} . \tag{22}$$

According to [20] there is one more exit condition for Newton's iteration, i.e., when the solution is outside the valid parametric domain $u \notin < u_{min}, u_{max}), v \notin < v_{min}, v_{max})$. This condition was not taken into account, because the intersection point is subjected to further tests, described in Section 2.2.6 which are more strict. In theory it can happen that the Jacobian is close to zero and its inverse tends to infinity. In this case either the surface is not regular or the ray is parallel to a silhouette ray at this point. As a consequence, the computed point is rejected or not found and a new ray is traced.

2.2.4 Bounding volume hierarchy

Newton's method for finding ray-surface intersection point is computationally expensive since it requires multiple evaluation of the surface point and surface derivatives (usually convergence achieved after 3–4 iterations). Therefore it is important to avoid ray-surface intersection test whenever possible. Additionally, Newton's method needs a good initial guess, which should be closer to the real solution for considerably curved surfaces.

Stated above requirements are met using the bounding volume hierarchy (BVH) described by Martin in [20]. Generally, the hierarchy consists of the root, as well as internal and leaf nodes. The root node is the highest level node containing the other ones. Leaf nodes are placed only at the lowest level of each hierarchy branch and are assigned initial point for Newton's iteration. Bounding volumes are more associated with the objects they are

actually bounding and have a tendency to bound them tightly, contrary to the other techniques like octrees, BSP-trees, KD-trees in which the space is divided using the top-down approach. For bounding volumes axis-aligned bounding boxes were chosen. They allow to use very efficient ray-box intersection algorithm introduced by Kay [29], mentioned later by Smits [30]. Axis-aligned boxes can also nicely bound flat parts of the surface which is often the case, as shown later in Section 3.

The method described by Abert [22,28] was used to create the bounding boxes, which are assigning the initial point for Newton's iteration and are leaf nodes in the hierarchy. The other nodes (root and internal) are created later during the stage of hierarchy development. In Abert's method the surface flatness criterion p is defined according to

$$p = \prod_{i=1}^{7} \mathbf{n}_i \cdot \mathbf{n}_{i+1} \ , \tag{23}$$

where $\mathbf{n}_i$ are surface normal vectors evaluated at eight points shown in Fig. 3.

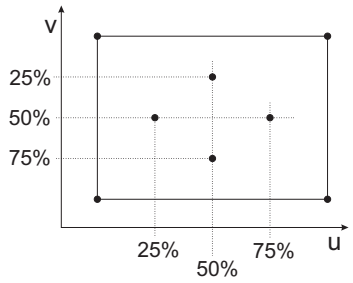

Figure 3: Black dots are points in parametric domain at which surface normals for surface flatness criterion are evaluated.

Surface is perfectly flat if $p = 1$. For $p > f$ a leaf bounding box is created by taking coordinates of four points corresponding to four limiting vertices of parametric domain. The initial point for Newton's iteration is the arithmetic mean of limiting values of parametric domain. If $p \leqslant f$ the surface is divided in half of its parametric domain. The process is recursively repeated till all subsurfaces fulfil the flatness criterion. Parameter $f \in < 0,1 >$ is set empirically and usually it is equal to 0.8–09. In case $p < 0$, the surface is also subdivided in half of the parametric domain. Examples of leaf bounding boxes created for two values of f parameter are shown in Figs. 4a and 4b.

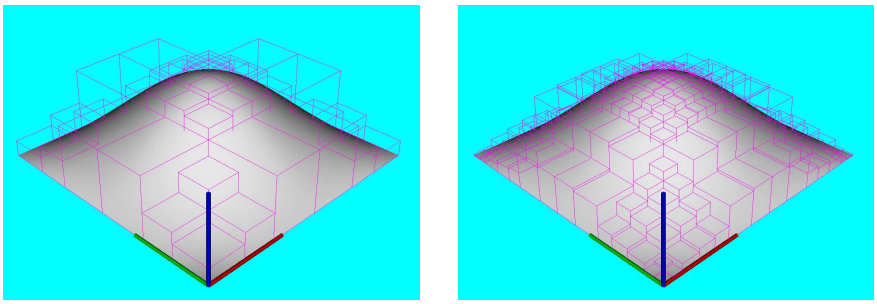

(a) $f = 0.8$ (b) $f = 0.95$

Figure 4: Leaf bounding boxes for NURBS surface created based on different surface flatness criterion parameter f.

By taking f parameter closer to 1 the parts of surfaces inside bounding boxes are 'more flat'. As a consequence higher number of bounding boxes is created leading to bigger hierarchy tree, higher memory consumption and slower ray traversal through the hierarchy. On the other hand, Newton's iteration is likely to converge faster.

After computing all the leaf bounding boxes the BVH is created using the Goldsmith-Salmon algorithm [31]. The quality measure for the hierarchy is the average time needed for a ray to traverse the hierarchy. The principle of the algorithm is to put the leaf nodes into the hierarchy tree one-by-one and to search the tree for optimum insertion place which is determined by the minimization of the tree cost function. The algorithm allows to create 'almost optimal' hierarchy tree and the time needed for it is of order $n \log(n)$, where n denotes the number of leaf nodes. An example of BVH is shown in Fig. 5.

In order to efficiently store and traverse the BVH a depth-first order array of bounding box objects with skip-pointer mechanism was used (Fig. 6). If the ray-box intersection test was successful, the next box to test is the subsequent element of the array. Otherwise, the box to test is determined by the skip-pointer mechanism which tells how many elements in front of the current element of the array should be omitted. The advantages of such representation of the hierarchy are efficient use of the computer memory (no empty elements), limited to the minimum the amount of information stored in one element and no need for using recursive function calls during the hierarchy traversal [30].

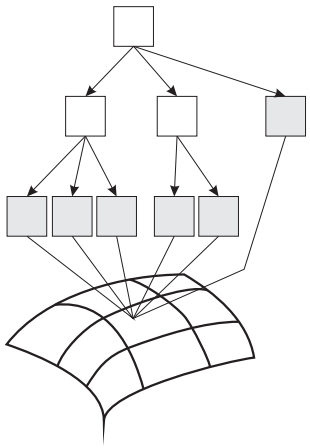

Figure 5: An example of BVH that is assigned to NURBS surface. Leaf nodes containing initial point for Newton's iteration are marked by grey colour.

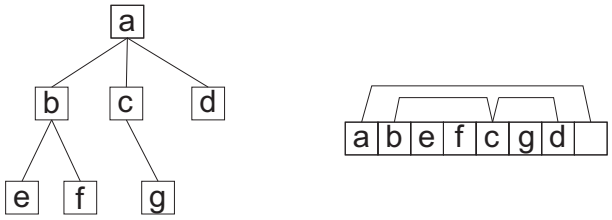

Figure 6: BVH representations: left – using pointers to child nodes, right – depth-first order array with skip-pointer mechanism.

2.2.5 Bundle emission point

An important step in MCRT method is determination of the bundle emission point. Since the paper deals with radiation problems without absorption/emission in gases the energy bundle can have its emission point only at boundary elements or precisely NURBS surfaces. The emission points should have uniform distribution across the surface, because the amount of energy emitted from the surface of constant temperature is proportional to its area. Algorithm that is capable of drawing random points on any parametric surface with uniform distribution was described by Kopytov in [32, 33].

A parametric surface $S(u, v)$ is defined in parametric domain $\mathbf{D} : \{u_1 \leqslant u \leqslant u_2;\ v_1 \leqslant v \leqslant v_2\}$. The joint probability distribution function of parameters u and v – $f(u, v)$ – is to be determined. This function corresponds to the uniform point distribution in 3D space. In case of uniform distribution

of points on the surface, the probability of point A being on the differential surface dS equals to

$$P\left(A \in dS\right) = \frac{dS}{S} \ , \tag{24}$$

where

$$dS = \sqrt{EG - F^2} dudv \ , \tag{25}$$

$$S = \iint\limits_{\mathbf{D}} \sqrt{EG - F^2} dudv \ . \tag{26}$$

E, F, G are coefficients of the first fundamental form of the surface S:

$$E = S_u \cdot S_u \ , \tag{27}$$

$$F = S_u \cdot S_v \ , \tag{28}$$

$$G = S_v \cdot S_v \ . \tag{29}$$

Inserting Eqs. (25) and (26) into (24) leads to

$$P\left(A \in dS\right) = \frac{\sqrt{EG - F^2} dudv}{\iint\limits_{\mathbf{D}} \sqrt{EG - F^2} dudv} \ , \tag{30}$$

where $\mathbf{D}$ is surface parametric domain. On the other hand, probability of point A being on the differential surface dS equals to

$$P\left(A \in dS\right) = f(u, v) dudv \ . \tag{31}$$

Comparing the Eqs. (30) and (31) the expression for unknown joint probability distribution function is found

$$f(u, v) = \frac{\sqrt{EG - F^2}}{\iint\limits_{D} \sqrt{EG - F^2} dudv} \ . \tag{32}$$

The function $f(u, v)$ is proportional to $\sqrt{EG - F^2}$.

Eguation (32) is used in the algorithm for drawing random points on parametric surface with uniform distribution in 3D space:

1. Determine the maximum of the function $f_{max} = \max \sqrt{EG - F^2}$ in domain $\mathbf{D}$.

2. Generate two random numbers R_u i $R_v \in < 0,1 >$ and scale them to the size of the domain $\mathbf{D}$ by computing parameters u_0, v_0:

$$u_0 = (u_2 - u_1)R_u + u_1, \quad v_0 = (v_2 - v_1)R_v + v_1 \ . \tag{33}$$

   where u_1, u_2, v_1, v_2 are local parameters bounding valid surface domain.

3. Check the condition

$$f_{max}R < f(u_0, v_0) \ , \tag{34}$$

   where R – random number from $< 0,1 >$. If the condition is fulfilled the point $S(u_0, v_0)$ is accepted, otherwise it is rejected.

4. Repeat steps 2, 3 till required number of points on the surface S is achieved.

The algorithm described above is applicable to one surface only, thus it needs upgrading to account for many surfaces, as it is the case for some of the boundary cells of ortho-Cartesian mesh. If boundary cell contains more than one NURBS surface, the surface is chosen randomly with probability proportional to its area. Kopytov's algorithm is used to draw a single emission point from this surface and then the point is tested if it lies inside the boundaries of ortho-Cartesian cell. If it does, it is accepted as an emission point for the new energy bundle, otherwise the procedure is repeated.

2.2.6 Interrogation of intersection points

In general, the bundle can have more than one intersection point with NURBS surface. All possible intersection points are found during BVH traversal in which, if the ray hits the leaf node, the iterative Newton's procedure is launched. The hierarchy is traversed till its end, because finding one ray-surface intersection point does not guarantee it is correct and unique. After BVH traversal by the ray the list of all possible intersection points is created. The task of the interrogation algorithm is to choose the closest point to the ray origin that is within current ortho-Cartesian cell. In case no point meeting all the criteria was found the ray goes to neighbouring ortho-Cartesian cell, according to mechanism described in Section 2.2.1.

It is important to note, that if the value of surface flatness criterion parameter f is set low, it is more probable for Newton's method to converge to improper point or even diverge. In this case the ray can travel to inactive

ortho-Cartesian cell and escape from the enclosure producing nonphysical result. This error does not terminate the code execution, simply the traced ray is neglected. It should be kept in mind that the value of f parameter is a compromise between the speed the ray traverses through BVH and the number of rays that can escape from the enclosure.

Another issue worth mentioning is the minimum distance of the intersection point from the bundle emission or reflection point L_{min}. It was noted that some intersection points were found exactly in the emission/reflection point. It is caused by the fact that just after emission or reflection the ray is inside the boundary cell and the procedure of finding intersection point is automatically triggered. After introducing L_{min} parameter the ray is forced to travel at least this distance before intersection is reported. The value of the L_{min} parameter is set by the user and it should be equal to several percent of mean linear dimension of ortho-Cartesian cell.

3 Results

This section describes three examples on which MCRT model was checked. The influence of the number of rays traced from one surface element on the solution accuracy is shown on the example of view factor. The cube example describes how the ortho-Cartesian mesh resolution affects the results. Finally, the MCRT model is used to perform a full thermal analysis of the pit furnace operation.

3.1 View factor estimation

MCRT model was used to estimate value of the view factor for two parallel rectangular plates of sides equal to X and Y. Surfaces lay in front of each other in distance L. The exact value of the view factor was calculated using the expression from [34]

$$F_{ij} = \frac{2}{\pi\bar{X}\bar{Y}}\left\{\ln\left[\frac{(1+\bar{X}^2)(1+\bar{Y}^2)}{1+\bar{X}^2+\bar{Y}^2}\right]^{1/2} + \bar{X}(1+\bar{Y}^2)^{1/2}\tan^{-1}\frac{\bar{X}}{(1+\bar{Y}^2)^{1/2}}\right\} + \frac{2}{\pi\bar{X}\bar{Y}}\left\{\bar{Y}(1+\bar{X}^2)^{1/2}\tan^{-1}\frac{\bar{Y}}{(1+\bar{X}^2)^{1/2}} - \bar{X}\tan^{-1}\bar{X} - \bar{Y}\tan^{-1}\bar{Y}\right\}, \tag{35}$$

where $\bar{X} = X/L$, $\bar{Y} = Y/L$. By setting the values $X = Y = 1/3$ m and $L = 1$ m the exact value of $F_{ij}^{exact} = 0.0329714$.

During the simulation rays were traced from the surface of one plate and hits were reported when rays arrived at the second plate. Using the number of hits reported and total number of rays traced the view factor F_{ij} can be estimated using the Eq. (6). For a given total number of rays traced, N_{rays}, 10 tests were performed for different seeds of random number generator (RNG). It allowed to estimate a mean value, $F_{ij}^{estimate}$, standard deviation, s_{10}, and relative error, ϵ, for the view factor. The results are listed in Tab. 1 and shown in the graph in Fig. 7.

Table 1: Results of simulation of view factor estimate. Values computed on the basis of 10 runs with different RNG seeds.

N_{rays}, –	F_{ij}^{exact}, –	$F_{ij}^{estimate}$, –	s_{10}, –	ϵ, %
100	0.0329714	0.047	0.02648	42.55
1000	0.0329714	0.0341	0.00370	3.42
10000	0.0329714	0.03310	0.00129	0.39
100000	0.0329714	0.033063	0.00043	0.28
1000000	0.0329714	0.0328263	0.00018	0.44

The results show that the estimated value of the view factor tends to an exact value with the increasing number of rays traced. The value of standard deviation for 10 samples decreases proportionally to the value of expression $\sqrt{N_{rays}}$. Also relative error tends to 0 for a large number of rays traced.

3.2 The cube

In this test the results obtained by S2S Ansys Fluent [35] and OpenFOAM MCRT models are compared on the geometry of cube that has edges equal to 1m (Fig. 8).

Fixed temperature boundary conditions are listed in Tab. 2, in which $T(r)$ is temperature profile on the wall

$$T(r) = \begin{cases} (T_0 - T_1)\cos^2(\frac{\pi}{2r_{max}}r) + T_1, & \text{if } r < r_{max} \ , \\ T_1 \ , & \text{otherwise} \ , \end{cases} \tag{36}$$

where: $r = \sqrt{p_i - p_0}$ – distance between the center of the cell boundary wall p_i and the center of *Z0* wall p_0; $T_0 = 500$ K, $T_1 = 300$ K – maximum and

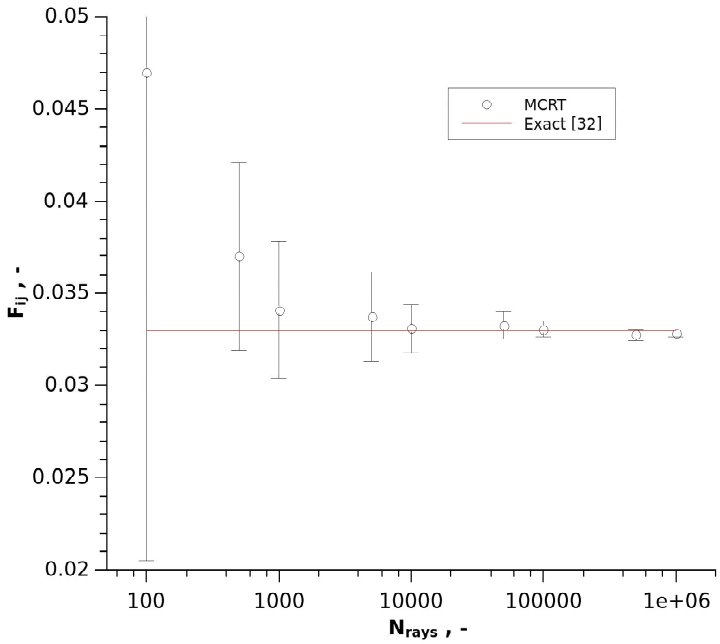

Figure 7: Estimates of the view factor F_{ij} for two parallel plates computed on the basis of 10 tests with various RNG seeds done with MCRT model for different number of rays traced N_{rays}.

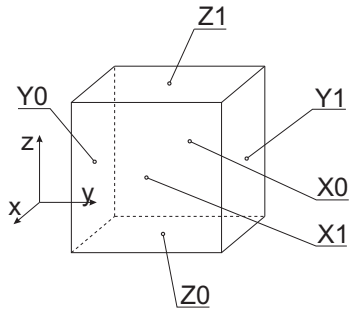

Figure 8: The geometry of 1m cube with names of boundary walls.

minimum temperature, $r_{max} = 0.4$ m – radius of influence. $T(r)$ function guarantees temperature continuity on the boundary walls.

CFD mesh consists of 125000 cells which corresponds to uniform x, y, z resolution of 50. MCRT model was run 5 times for different RNG seeds for each otho-Cartesian mesh resolutions M_{res} equal to 10, 20 and 40. The

Table 2: Boundary conditions – temperature and absorptivity for the case of 1m cube.

Wall name	T, K	α, –
X0, X1, Y0, Y1, Z1	300	1
Z0	$T(r)$	1

number of rays traced from one surface element was 10000.

Table 3 shows balances of radiative heat fluxes computed by S2S model and MCRT for three ortho-Cartesian mesh resolutions. The results produced by MCRT model follow S2S results and are closer to them for the greater ortho-Cartesian mesh resolution. The balance of radiative heat fluxes for the entire enclosure should be equal to zero. In the case of MCRT model it is greater than for S2S model, but the Monte Carlo results converge with the increase of mesh resolution. The unbalance is caused by uncertainties in computation of radiation distribution factors. The uncertainties can be lowered either by increasing the number of energy bundles traced, or by smoothing of the distribution factor matrix. The smoothing procedure causes the elements of distribution factor matrix to fulfil energy conservation and reciprocity rules given by Eqs. (2) and (3). Current version of MCRT model has not the smoothing procedure implemented yet.

Table 3: Balance of radiative heat fluxes, (W), at cube walls for S2S and MCRT models. In the case of MCRT model the results are average values of 5 runs for different RNG seeds.

Model	M_{res}	X0	X1	Y0	Y1	Z0	Z1	Net
MCRT	10	-60.72	-61.20	-59.38	-62.08	314.02	-71.78	-1.13
MCRT	20	-61.59	-63.05	-62.40	-63.32	323.43	-77.09	-4.03
MCRT	40	-62.58	-62.04	-62.39	-62.94	325.85	-76.55	-0.65
S2S	–	-62.76	-62.75	-62.77	-62.76	326.53	-75.52	-0.03

Figure 9 shows the influence of ortho-Cartesian mesh resolution M_{res} on the radiative heat fluxes. Increasing the resolution causes the solution to be more smooth and to approach the reference solution of S2S model. Moreover, the lower the resolution, the bigger the difference between extreme values of radiative heat flux reported by S2S and MCRT models. This fact

is caused by the temperature averaging inside the ortho-Cartesian cells and it is important, since the radiative heat flux is proportional to fourth power of temperature.

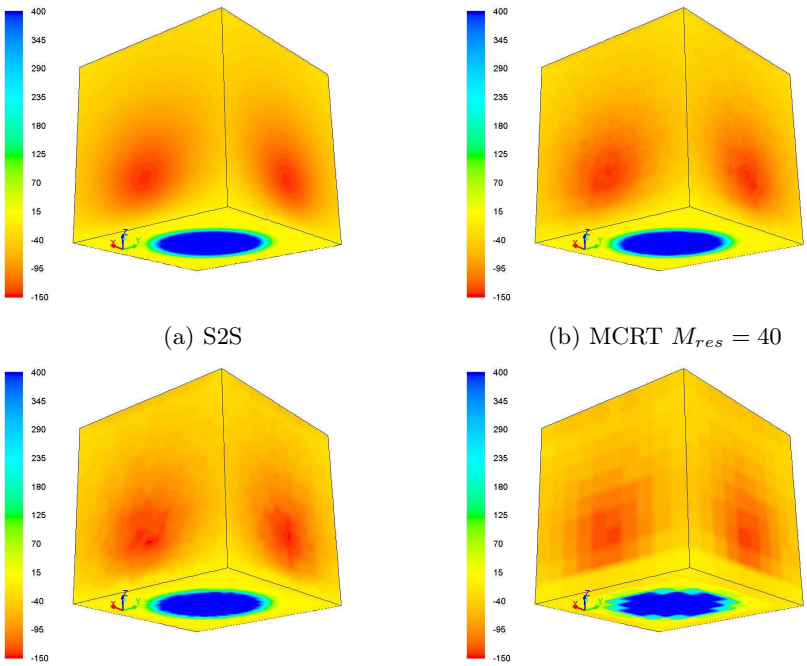

(a) S2S (b) MCRT $M_{res} = 40$

(c) MCRT $M_{res} = 20$ (d) MCRT $M_{res} = 10$

Figure 9: The influence of ortho-Cartesian mesh resolution on the radiative heat fluxes (W/m^2) on the walls.

In order to measure how the solution of MCRT model deviates from the accurate solution of S2S model the radiative heat fluxes on the line of symmetry of X0 wall were extracted and compared using *p-norms*. The norms are defined as follows:

$$||\mathbf{x}||_p = \left(|x_1|^p + |x_2|^p + ... + |x_n|^p\right)^{1/p}, \tag{37}$$

$$||\mathbf{x}||_\infty = \max\left\{|x_1|, |x_2|, ..., |x_n|\right\}, \tag{38}$$

where: $p = 1, 2$, $x_i = x_i^{S2S} - x_i^{MCRT}$. The results are summarized in Tab. 4. Increasing the ortho-Cartesian mesh resolution two times causes the norms to decrease by a factor of two and to improve the accuracy of the MCRT model. It should be noted that the resolution of ortho-Cartesian mesh can not be greater than the resolution of CFD mesh.

Table 4: The influence of ortho-Cartesian mesh resolution on the deviation of heat fluxes on symmetry line of X0 wall obtained using MCRT model from S2S solution and expressed in form of *p-norms.*

M_{res}	$\|\|\mathbf{x}\|\|_\infty$	$\|\|\mathbf{x}\|\|_1$	$\|\|\mathbf{x}\|\|_2$
10	11.9	239.3	39.4
20	9.4	130.2	24.3
40	3.4	59.3	10.7

3.3 Pit furnace

In order to test MCRT model in practical case, the technique was used for simulation of the pit furnace performance. This kind of furnaces are used (among other processes) for nitriding process of metal parts, such as connecting-rods, gear wheels, sleeves, housings, etc. As a result of nitriding, a coating is created on the outer surface of the material. The coating has a high hardness and good antiwear properties. The nitriding process is operated in controlled atmosphere of 20% ammonia, 80% nitrogen mixture and in temperatures between 753 and 973 K. Depending on the required thickness of coating and the type of material, the whole process can last from several hours to a couple of days. Simulation covered the steady-state stage of the nitriding process.

The cross-section of the cylindrical pit furnace in the vertical plane of symmetry is shown in Fig. 10. The cylindrical chamber *14* of the pit furnace has the working space of dimensions: diameter ϕ 600 mm and height 900 mm and is closed by a removable lid at the top. The sides of the chamber are covered by electric heaters *1–10* which have a maximum power of 40 kW. The furnace is insulated by bricks *12* and ceramic blankets *15*. Steel legs *11* reinforce the furnace base on which a steel shaft *13* is placed. Ammonia/nitrogen mixture flows to the chamber through the inlet *18* and escapes through the outlet *16*. The mixing fan shaft *17* is placed in the center of the lid.

It should be noted that during the creation of the geometrical model of the furnace certain simplifications and assumptions were made including:

- placing heaters inside the insulation,
- neglecting the presence of the gas-tight retort,

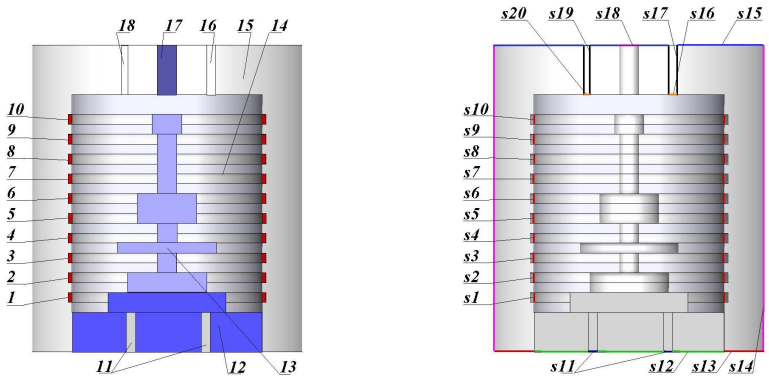

(a) (b)

Figure 10: Cylindrical furnace cross-section through vertical plane of symmetry: *1–10* – electric heaters, *11* – steel legs, *12* – insulating brick, *13* – shaft, *14* – chamber, *15* – insulating ceramic blankets, *16* – outlet, *17* – fan shaft, *18* – inlet, *s1-s10* – inner surfaces of electric heaters, *s11* – bottom surface of steel legs, *s12* – bottom surf. of insulating brick, *s13, s14, s15* – bottom/side/top surface of insulating blanket, *s16, s20* – outlet/inlet, *s17, s19* – outlet/inlet pipes walls, *s18* – top surf. of fan shaft. The furnace data acquired from Seco/Warwick Group, [36].

- neglecting the presence of the fan.

In practice, the furnace load is placed inside the gas-tight retort which prevents the heaters to have the contact with nitriding atmosphere. The usage of the fan causes the atmosphere and its temperature to be more uniform inside the retort and especially in the neighbourhood of surfaces undergoing nitrification which influence quality of the process. It should be kept in mind that the introduced simplifications influence the flow of the nitriding mixture inside the chamber. They do not change the overall energy balance of the system and are not crucial for testing the MCRT radiation model. Because of the low optical thickness of the medium inside the chamber, the absorption/emission properties of ammonia/nitrogen mixture were neglected.

Selected boundary conditions are named in Fig. 10b and listed in Tab. 5. Material properties are shown in Tab. 6. The emissivity of all walls inside the furnace chamber was set to 1. The simulation was run for two radiation mode MCRT and S2S for comparison.

As a result of the simulation temperatures and radiative heat fluxes within the chamber were determined and overall energy balance of the fur-

Table 5: Boundary conditions for the case of pit furnace. Names correspond to the numeration introduced in Fig. 10b.

Name	BC type	Property	Units	Value
s11, s12, s13, s14, s15, s18	wall natural convection	T_{ext} h_{ext}	K W/m^{2}K	300 5
s16	pressure outlet	p	Pa	0
s20	velocity inlet	v $\dot{V}$ T	m/s l/min K	0.0853 10 300
s17, s19	wall	q	W/m^2	0
1 – 10	volume	q_v	W/m^3	130000

T_{ext} – external free-stream temperature, h_{ext} – external heat transfer coefficient, p – pressure, v =– velocity, $\dot{V}$ – volumetric flow rate, T – temperature, q – surface heat flux, q_v – volumetric heat source.

Table 6: Material properties used in the simulation. Volumes numbering corresponds to one introduced in Fig. 10a.

Material	Volumes	k, W/mK	ρ, kg/m^3	c_p, J/kgK
steel	11, 13, 17	58.00	7800	600
insulating blanket	15	0.20	70	970
insulating brick	12	0.14	480	1050
heaters rod	1–10	80.00	8000	450

k – heat conductivity, ρ – density, c_p – heat capacity.

nace was calculated. Figure 11a shows the resulting temperature profile in the plane of symmetry. The detailed inspection of the profile reveals the existence of thermal bridges, created by fan shaft and steel legs. Also the cold stream of ammonia/nitrogen mixture, close to the inlet is visible. Figure 11b shows the radiative heat fluxes on the sides of the chamber. Although the duty of each heater is the same, their radiant power differs significantly. This fact is caused by the different temperatures of the heaters. The heaters *1* and *10* have the lowest temperature and corresponding radiant power. The temperature and radiative heat flux profiles on the

surface of nitriding object are shown in Fig. 12. The temperature on the shaft equals to 967 ± 4 K and its range is too wide to assure the quality of the process. The nonuniform temperature is caused by the cold stream of ammonia/nitrogen mixture and exposure to the low-temperature side of the fan shaft. Uniformity of the temperature distribution (and simultaneously nitrogen concentration) can be improved by using fan and gas flow-distribution equipment. Moreover, the electric power input for each heater should be adjusted in order to maintain uniform temperature across the chamber.

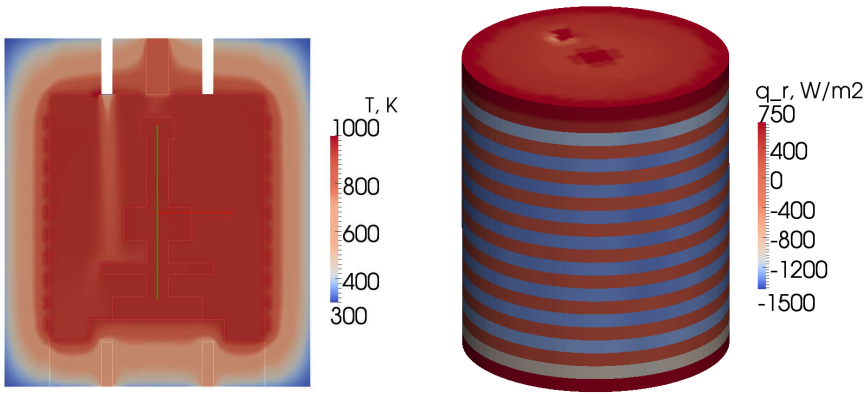

(a) (b)

Figure 11: (a) Temperature profile (T) in furnace cross-section through vertical plane of symmetry. (b) Radiative heat flux (q_r) on the outer sides of cylindrical chamber.

The overall energy balance for the furnace is shown in Tab. 7. In order to maintain the required temperature inside the chamber in steady state, only 10% of maximum heaters duty is needed. It is clear that most of the heat is lost through the insulation and metal parts and only a small percent ($< 4\%$) by hot exhaust gases. Mean temperature outside the side insulation is 382 K which is too high for people who operate the furnace. Additional cooling device should be installed in order to avoid contact with hot surfaces.

The comparison of radiative heat flux, mean temperature on selected walls and heat fluxes from Tab. 7 done for MCRT and S2S models shows that the differences are less than 5%. The differences are caused mainly by the temperature averaging inside ortho-Cartesian cells done in MCRT model.

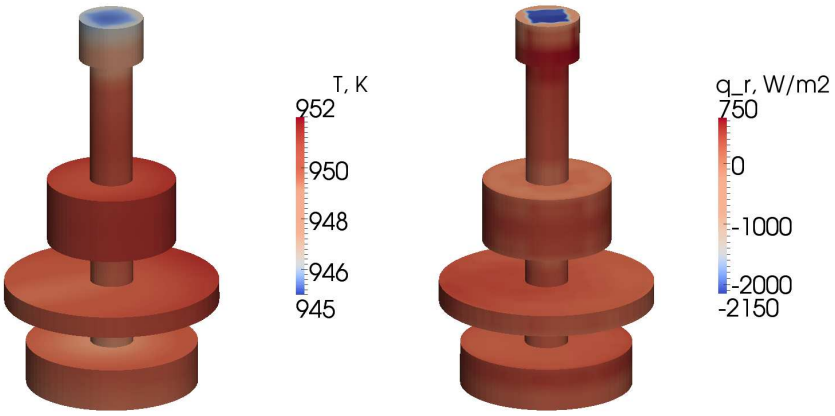

(a) (b)

Figure 12: Temperature (a) and radiative heat flux (b) profiles on the outer surface of the shaft.

Table 7: Overall energy balance of the furnace for MCRT and S2S models. Surface names correspond to ones introduced in Fig. 10b.

Surfaces	Q_{MCRT}, W	Q_{S2S}, W
s11, s12, s13	-508	-522
s14	-2761	-2766
s15, s17, s18, s19	-489	-469
s16, s20	-79	-108
H_{gas}	-137	-136
$Q_{heaters}$	4000	4000
Net	-26	1

4 Conclusions and summary

Radiation heat transfer model using Monte Carlo ray tracing method on hierarchical ortho-Cartesian meshes and NURBS surfaces for description of boundaries has been developed and discussed. The code is an add-on to the open-source CFD program OpenFOAM. The ortho-Cartesian mesh is constructed based upon the CFD mesh. Algorithms for finding ray-NURBS surface intersection and determining random, uniformly distributed loca-

tions of rays leaving NURBS surfaces are described. The presented version of the model does not account for the radiation absorption/emission within gases. However, the ultimate aim of the work is to upgrade the functionality of the model to problems in absorbing, emitting and scattering medium.

The developed model is tested on three examples with an assumption of gray diffuse walls: view factor, the cube and pit furnace. The results show how the number of rays traced from boundary element and the ortho-Cartesian mesh resolution influence the solution. Moreover, model ability to deal with geometries of complex shapes is proved. Wall heat fluxes and temperature predictions obtained by MCRT model are in good agreement with the S2S Fluent model.

Acknowledgements This research was sponsored by the National Research and Development Centre of Poland through the Strategic Program *'Advance technologies of energy generation'*, Research Task 2: 'Development of oxyfuel combustion technologies for pulverized and fluidized coal-fired boilers integrated with the carbon capture and storage technology', Grant No. SP/E/2/666420/10. The authors also thank dr inż. Łukasz Piechowicz and mgr inż. Andrzej Miliszewki from Seco/Warwick Europe S.A. for support in the field of furnace construction and operation.

Received 15 February 2014

References

[1] Mahan J.R.: *Radiation Heat Transfer: A Statistical Approach.* John Wiley & Sons, New York 2002.

[2] Modest M.F.: *Radiative Heat Transfer, 2nd Edn.* Academic Press, 2003.

[3] Zeeb C.N., Burns P.J., Branner K., Dolaghan J.: *User's manual for MONT3D-Vers. 2.4.* Department of Mechanical Engineering. Colorado State University, Fort Collins 1999.

[4] OpenFOAM. www.openfoam.com.

[5] Fujimoto A.: *Accelerated Ray Tracing.* In: Proc. Computer Graphics, Tokyo 1985, 41–65.

[6] Fujimoto A., Tanaka T., Iwata K.: *ARTS: Accelerated Ray-Tracing System.* IEEE Comput. Graph. **6**(1986), 4, 16–26.

[7] Amanatides J., Woo A.: *A Fast Voxel Traversal Algorithm for Ray Tracing.* In: Proc. Eurographics Conf., 1987.

[8] Węcel G.: *Mathematical Modelling of Coupled Radiative and Convective Heat Transfer.* PhD. thesis. Silesian UT, Institute of Thermal Technology, Gliwice 2003.

[9] Białecki R.A., Węcel G.: *Solution of conjugate radiation convection problems by a BEM FVM technique.* J. Quant. Spectrosc. Radiat. Transf. **84**(2004), 539–550.

[10] Zeeb C.N., Dolaghan J.S., Burns P.J.: *An efficient Monte Carlo particle tracing algorithm for large, arbitrary geometries.* Numer. Heat Tr. B-FUND **39**(2001), 4, 325–344.

[11] Mazumder S.: *Methods to accelerate ray tracing in the Monte Carlo Method for surface-to-surface radiation transport.* J. Heat Transf. **128**(2006), 9, 945–952.

[12] Glassner A.S.: *Space subdivision for fast ray tracing.* IEEE Comput. Graph. **4**(1984), 10, 15–22.

[13] Jansen F. W.: *Data structures for ray tracing.* In: (L.R.A. Kessener *et al.*, Eds.) Data structures for raster graphics. Springer-Verlag, Berlin 1986, 57–73.

[14] Piegl L., Tiller W.: *The NURBS Book, Monographs in Visual Communication*, 2nd Edn. Springer-Verlag, Berlin Heidelberg 1997.

[15] Farin G.: *Curves and Surfaces for Computer Aided Geometric Design: A Practical Guide.* Academic Press Inc., New York 1990.

[16] Pabst H.F., Springer J.P., Schollmeyer A., Lenhart R., Lessig C., Froehlich B.: *Ray casting of trimmed NURBS surfaces on the GPU.* In: Proc. Interactive Ray Tracing 2006, IEEE Symposium, 2006, 151–160.

[17] Whitted T.: *An improved illumination model for shaded display.* Commun. ACM. **23**(1980), 6, 343–349.

[18] Rubin S.M., Whitted T.: *A 3-dimensional representation for fast rendering of complex scenes.* Comput. Graphics **14**(1980), 3, 110–116.

[19] Toth D.L.: *On ray tracing parametric surfaces.* Comput. Graphics **19**(1985), 3, 171–179 (SIGGRAPH '85 Proc.).

[20] Martin W., Cohen E., Fish R., Shirley P.: *Practical ray tracing of trimmed NURBS surfaces.* J. Graph. Tools **5**(2000), 1, 27–52.

[21] Geimer M., Abert O.P.: *Interactive ray tracing of trimmed bicubic Bézier surfaces without triangulation.* In: Proc. 13th Int. Conf. in Central Europe on Computer Graphics, Visualizaction and Computer Vision WSCG 2005, 71–78.

[22] Abert O.P., Geimer M., Muller S.: *Direct and fast ray tracing of NURBS surfaces.* In: Proc. Interactive Ray Tracing 2006, IEEE Symposium, 2006, 161–168.

[23] Kajiya J.T.: *Ray tracing parametric patches.* Comput. Graphics **16**(1982), 3, 245–254 (SIGGRAPH '82 Proc.).

[24] Nishita T., Sederberg T.W., Kakimoto M.: *Ray tracing trimmed rational surface patches.* Comput. Graphics **24**(1990), 4, 337–345.

[25] Efremov A., Havran V., Seidel H. P.: *Robust and numerically stable Bézier clipping method for ray tracing NURBS surfaces.* In: Proc. 21st Spring Conf. on Computer Graphics SCCG'05, 2005, 127–135.

[26] Wang S. W., Shih Z. C., Chang R. C.: *An efficient and stable ray tracing algorithm for parametric surfaces.* J. Inf. Sci. Eng. **18**(2001), 541–561.

[27] Point Cloud Library. http://pointclouds.org/

[28] Abert O. P.: *Interactive ray tracing of NURBS surfaces by using SIMD instructions and the GPU in parallel.* MSc. thesis. Univ. of Koblenz-Landau 2005.

[29] Kay T. L., Kajiya J. T.: *Ray tracing complex scenes.* Comput. Graphics **20**(1986)(SIGGRAPH '86 Proc.), (D.C. Evans, R.J. Athay, Eds.), 269–278 .

[30] Smits B.: *Efficiency issues for ray-tracing.* J. Graph. Tools **3**(1998), 2, 1–14.

[31] Goldsmith J., Salmon J.: *Automatic creation of object hierarchies for ray tracing.* IEEE Comput. Graph. **7**(1987), 5, 14–20.

[32] Kopytov N.P., Mityushov E.A.: *Mathematical model of reinforcement of shells made of composite materials and problem of uniform distribution of points on surfaces.* Vestnik PGTU. Mechanika **4**(2010), 55–66 (in Rusian).

[33] Kopytov N.P., Mityushov E.A.: *The universal algorithm of uniform distribution of points on arbitrary analytic surfaces in three-dimensional space.* Fund. Res. **4**(2013), 618–622.

[34] Cengel Y.A.: *Heat Transfer: A Practical Approach, International Edition*, 2nd Edition. McGraw-Hill, 2003.

[35] ANSYS Inc. www.ansys.com.

[36] Seco Warwick Poland: www.secowarwick.com/pl